Variability in timing of a β-catenin pulse biases a stochastic cell fate decision in *C. elegans*

Jason R. Kroll, Jasonas Tsiaxiras, and Jeroen S. van Zon[1]

AMOLF
Science Park 104
1098 XG, Amsterdam
The Netherlands

Summary

Stochastic cell fate decisions occur frequently during animal development. In many cases, individual cells randomly choose one cell fate out of a limited repertoire of fates, but with the relative frequency of the different possible fates tightly controlled. To address how signaling networks enable cell-autonomous stochastic decisions and the network properties that control the relative frequency of the resulting cell fates, we studied the stochastic differentiation of the *C. elegans* P3.p cell. We used time-lapse microscopy to measure the single-cell dynamics of BAR-1/β-catenin and LIN-39/Hox, two key regulators of the network, while monitoring the cell fate decision. Surprisingly, the timing of the decision is highly regulated, even in mutants that drastically alter the frequency of the cell fates. Using experimental data and modeling approaches, we found that a combination of variability in LIN-39 levels and variability in the timing of BAR-1/β-catenin signaling activation are significant noise sources that bias the stochastic decision. Our results highlight that temporal aspects of Wnt signaling can provide sufficient variation in a signaling network to enable a cell-autonomous stochastic cell fate decision in a multicellular organism.

Keywords

cell fate, differentiation, *C. elegans*, stochasticity, noise, variability, single-cell, Wnt, Hox, β-catenin, pulses

[1] Corresponding author (J.v.Zon@amolf.nl)

Introduction

One fundamental question concerning development is how cells can robustly obtain the correct cell fate and give rise to a viable organism despite molecular noise and stochasticity in the environment. It is usually assumed that suppressing this variability is essential for stereotypical development. Upon closer look, however, variability among cells that leads to stochastic or variable cell fate outcomes is a cornerstone of many processes that shape development. Additionally, despite being stochastic in nature, fate outcomes are often assumed at a defined frequency on the population level. For example, a specific portion of cells in the early mouse embryo show stochastic expression of the essential regulator *Nanog* (Dietrich and Hiiragi, 2007). Additionally, in the photoreceptor cells in the retina, each cell stochastically chooses one photopigment gene to express from a total of three, but each photopigment gene appearing at a defined frequency in the total population of photoreceptor cells (Roorda and Williams, 1999; Smallwood et al., 2002). A common theme from these systems emerges: that the outcome of each individual decision is random, but relative frequency of different fates is highly regulated.

Currently, stochastic cell fate decisions are best understood in context of single-celled systems, where gene expression noise has been identified as the primary source of variation responsible for alternate cell fates. One early finding is that intrinsic noisy expression in master regulators regulates the fate and antibiotic-resistance in *B. subtilis* cells (Balaban, 2004; Losick and Desplan, 2008; Maamar et al., 2007; Süel et al., 2006). Additionally, noise in gene expression bursts was responsible for cell-fate switching in *S. cerevisiae* (Kaufmann et al., 2007).

From study of these systems, a general model emerges to explain how different discrete cell fate can result from random molecular fluctuations (Fig. 1a). Initial variability in an element is then transformed into a bimodal distribution by factors or regulators acting downstream in the genetic network, which transforms the variability in one element to a discrete outcome. In this picture, the relative frequency of cell fate can be changed by many factors, such as reduction or loss of a regulator, causing the distribution to shift and favor one cell fate over the rest (Fig. 1a, orange dashed line). However, it is currently not clear how stochastic cell fate decisions are regulated during animal development, since cell fate decisions in multicellular organisms are inherently different than single-celled systems due to the temporal constraints of developmental timing, requirements of external inductive signals, and the possible influence of neighboring cells in the tissue or vicinity. Therefore, cell fate decisions that are determined only by noisy gene expression seem inadequate to fully explain how a stochastic decision could be coordinated in a multicellular organism. Most importantly, the embryo needs the ability to precisely tune relative frequency of different cell fates in space and time. Currently it is not know how this is achieved on the molecular level.

Developmental regulation of relative cell fate frequency is best understood in stochastic cell fate decisions involving cell-cell communication by Notch signaling. For example, lateral

inhibition, in which cells inhibit neighboring cells via Notch/Delta interactions, reduces variability in the cell fate ratios and establishes cell fate frequencies based on geometry, such as the number of cells contacting their neighbors. This phenomena occurs in many situations during development, such as the AC/VU decision in *C. elegans* or the selection of secretory cell fate in the intestine (Tóth et al., 2017; Wilkinson et al., 1994).

However, most stochastic cell fate decisions are cell-autonomous. It is poorly understood what features of signaling network responsible for amplifying random variability into cell fate at a specific time of development and what parameters of network modified to tune relative frequency. Two key elements are missing for understanding: first, the ability to quantify variability in a signaling network, and second, techniques to follow the decision-making process in time, to see what aspects of variability correlate with final cell fate outcome. We overcome these obstacles by studying a simple, stochastic cell fate decision in *C. elegans*, the decision between hypodermal and vulva precursor cell (VPC) fate in the P3.p cell (Figure 1b). Here, we make use of an approach we developed recently to follow the dynamics of signaling pathways in single-cells in developing *C. elegans* larvae (Gritti et al., 2016) to examine the mechanisms and processes that are involved in a stochastic cell fate decision. Moreover, the system is well-suited to study regulation of relative cell fate frequency, as many mutants exist in which frequency of the fates are changed.

The P3.p cell is a member of the vulval precursor cell (VPC) competence group which is defined by its ability to form the vulva. The VPC competence group is made up of six cells named P3.p-P8.p (or Pn.p), which are located in the ventral nerve cord and are patterned to various vulval cell fates dby multiple signaling pathways (Eisenmann et al., 1998; Félix, 2012; Gleason et al., 2002; Gupta et al., 2012; Hill and Sternberg, 1993; Sternberg and Horvitz, 1986). The hypodermal or VPC stochastic cell fate decision occurs during the L2 stage of nematode development, in which the hypodermal fate arises through a fusion event in which the P3.p cell fuses to a neighboring cell (hyp7) (Shemer and Podbilewicz, 2002; Sternberg and Horvitz, 1986). In other animals, the cell does not fuse and remains as a VPC-fated cell, allowing for unambiguous determination of the frequency of each particular cell fate (Fig. 1b).

Many distinct signaling pathways have been identified that alter the frequency of the hyp7/fusion fate. The Hox genes are a conserved and essential class of developmental regulators of cell fate and developmental patterning (Koh et al., 2002; Salser et al., 1993). Mutations in the *C. elegans* Hox gene *lin-39* have been shown to impact the Pn.p cell fate frequencies due to its major role in the regulation of Pn.p cell competence, promotion of cell division, and repression of cell fusion (Clark et al., 1993; Koh et al., 2002; Maloof and Kenyon, 1998; Roiz et al., 2016; Shemer and Podbilewicz, 2002). In parallel, the Wnt/β-catenin signaling pathway is also required for the competence of the Pn.p cells (Gleason et al., 2002; Myers and Greenwald, 2007). The Wnt pathway is a highly conserved signaling pathway that regulates many developmental events and cell fates (Hirabayashi, 2004; Hudson et al., 2013; Lindström et al., 2014; Mucenski et al., 2003; Ohyama, 2006). In the canonical pathway, when Wnt ligands are present and detected by Wnt receptors in a particular cell, the transcriptional co-activator β–catenin (*bar-1*) accumulates, enter the nucleus, and co-regulates gene expression (Eisenmann

et al., 1998; Korswagen, 2002; Korswagen et al., 2000; Sawa and Korswagen, 2013). Mutations that decrease Wnt pathway activity cause an increase in hyp7/fusion fate frequency. Previous investigations into the P3.p cell fate decision showed the P3.p cell is extremely sensitive to the levels of Wnt ligands, suggesting that noise or variability in the gradient or distribution of ligands could provide the variation required to cause a stochastic cell fate decision (Pénigault and Félix, 2011a, 2011b). However, the activities of components of the Wnt pathway in the Pn.p cells are largely unexplored, which could introduce variability or noise into the system.

For the first time we followed individual cells during the cell fate decision process to directly observe and correlate gene expression and signaling activity to cell fate outcome during a cell autonomous cell fate decision. Using this approach we discovered that the outcome of the decision was temporally regulated, with a mechanism in place to ensure that the decision is executed at the proper time of development that is independent of the frequencies of each cell fate. In addition, we characterized potential sources of noise and variability and identified that each acts with different mechanisms to bias the cell fate decision. Expression levels in *lin-39* played a minor role in biasing the cell fate outcome in parallel with the Wnt pathway. The Wnt ligand *cwn-1* itself introduced significant variability into the Wnt response, and we found that the level of Wnt ligands controlled the temporal duration of β-catenin accumulation rather than the accumulation rate. Using mathematical modeling and simulations, we find that noise and variability in the timing of the onset of the Wnt/ β-catenin pathway activity biases the cell fate decision. Overall, we present a model for a cell-autonomous and stochastic cell fate decision that can be tuned and regulated without disrupting temporal aspects, an essential feature for proper development.

Results

Time-lapse microscopy of a stochastic cell fate decision

So far, whether P3.p undergoes fusion or assumes VPC fate in wild-type or mutant animals has been assessed only after the process has completed (Alper and Kenyon, 2001, 2002; Chen and Han, 2001; Eisenmann et al., 1998; Myers and Greenwald, 2007; Pénigault and Félix, 2011a, 2011b). To correlate early stochastic molecular events to eventual cell fate outcome it is essential to follow these processes directly in time. Here, we utilize a novel fluorescent time-lapse microscopy approach that makes it possible to study single-cell dynamics inside *C. elegans* larvae for their entire ~40 h development (Gritti et al., 2016) We tested whether we could directly observe P3.p fusion dynamics inside single animals. We used two independent measures of cell fusion: first, the apical junction protein AJM-1, which accumulates in Pn.p cells but is degraded upon cell fusion (Brabin et al., 2011). Second, flow of GFP from the hypodermis into the fusing cell, using animals carrying an extrachromosal array that targets GFP expression to the hyp7 hypodermal syncytium. In all animals, we saw that AJM-1::mCherry in the P3.p cell expanded along the A-P direction during the early L2 larval stage, until it made contact with AJM-1::mCherry in P4.p after ~5 h (Supplementary Movies 1-2, Fig. 1c,d), as observed before (Shemer et al., 2004). This was followed by a pronounced ruffling of the AJM-1:mCherry signal and a rapid retraction of AJM-1::mCherry towards the posterior, with the fluorescence signal fully disappearing from P3.p within ~1hr (Fig. 1c,d). Inflow of GFP from the hypodermis into P3.p was observed as soon as AJM-1::mCherry retraction commenced (Fig. 1c,d,e), showing that the changes in AJM-1 were not a delayed response to but instead coincided directly with P3.p fusion. For this reason and because the AJM-1 signal could be easily monitored in parallel with other fluorescent reporters in the same channel, we used AJM-1 dynamics to establish (timing of) P3.p fusion for all subsequent experiments.

Even though changes to the frequency of P3.p hyp7/fusion versus VPC fate in mutants are well studied (Alper and Kenyon, 2001, 2002; Chen and Han, 2001; Eisenmann et al., 1998; Myers and Greenwald, 2007; Pénigault and Félix, 2011a, 2011b), it was not known how such mutants impact the timing of this decision (Fig. 1f). We envisioned two opposing scenarios for how changes in P3.p fusion frequency could impact timing of fusion, depending on the mechanism underlying the stochastic cell fate decision. In the 'integrator' model, P3.p would integrate over a stochastically varying input signal, presumably Wnt signaling, by the slow stochastic accumulation of a downstream signal. Fusion would occur once the level of this signal passes a particular threshold. In such a model, mutants in which P3.p fusion frequency is increased would also exhibit fusion significantly earlier (Supplementary Fig. 1a). In contrast, in the 'snapshot' model, P3.p cells would make an instantaneous measurement of the stochastically varying input signal, with P3.p fusion occurring only when the input exceeds a threshold. In this scenario, changes in frequency would not affect timing of P3.p fusion (Supplementary Fig. 1b). We quantified the time of P3.p fusion in wild-type animals, carrying only the AJM-1::GFP reporter, and found that cell fusion occurred in a relatively narrow time window at 40-60% of the L2 larval stage (Fig. 1g). We then examined *bar-1(0)*, *cwn-1(0)* and *lin-*

39(lf) mutants, in which P3.p fusion frequency is significantly increased (Fig. 1f,g). We found that in these mutants P3.p fusion occurred within the same time window as wild-type animals, with only small differences between wild-type and mutant animals in average timing (Supplementary Fig. 1c). In these mutants often additional Pn.p cells, such as P4.p, assume hypodermal fate and fuse (Fig. 1f,g). Strikingly, even though the exact time of fusion can vary as much as 2 h between animals, when multiple VPCs fuse in a single animal, they typically do so at the same time (Fig. 1h). This is strong evidence that the stochastic decision between hypodermal and VPC fate is triggered by a global signal that impacts multiple Pn.p cells simultaneously. In general, these results show that cell fate frequency is regulated independently of its exact timing, favoring a 'snapshot' model as its control mechanism. How such a model might be implemented on the molecular level is discussed further below.

Bimodal *eff-1* expression precedes P3.p fusion

It is generally assumed that stochastic cell fate decisions are preceded by bimodal expression of cell date determinants (Fig. 1a) (Gamba et al., 2015; Wernet et al., 2006). Currently, it is not known if and where in the signaling network that controls the hyp7/fusion versus VPC fate decision such a bimodal distribution arises. To examine this, we used single-molecule fluorescent *in situ* hybridization (smFISH) to characterize the expression of the downstream-most effector of P3.p fusion, *eff-1,* a fusogenic protein that is necessary and sufficient to cause cell fusion (Mohler et al., 2002; Shemer et al., 2004). EFF-1 is a transmembrane protein that is required for most epithelial cell fusions in *C. elegans*, and is required on the plasma membrane of both cells that will fuse, in this case, the Pn.p cell and the hyp7 plasma membrane (Zeev-Ben-Mordehai et al. 2014; Smurova and Podbilewicz 2016;). We wanted to differentiate between two hypotheses: first, that *eff-1* is expressed in a bimodal manner, with low *eff-1* mRNA levels in P3.p cells that assume VPC fate, but high *eff-1* mRNA levels just prior to fusion in P3.p cells that assume hyp7/fusion fate. Alternatively, *eff-1* expression exhibits a broad, continuous distribution, with only those cells where *eff-1* levels rise above a threshold fuse. In *ajm-1::GFP* animals we quantified *eff-1* mRNA levels in animals where P3.p had not undergone fusion, based on presence and unruffled appearance of the AJM-1 signal (Fig. 2a,b). As animals were fixed for the smFISH protocol, they consisted of two classes between which we could not distinguish: those where P3.p would have assumed VPC fate and never fused and those where P3.p would have assumed hyp7/fusion fate but had not yet fused. Consistently, we found that in most animals *eff-1* mRNA was present in P3.p at low levels, ~5 molecules, similar to the level observed in P4.p, which never fuses (Fig. 2a,c). However, in the range of body lengths (340-380 µm) corresponding to the measured time of fusion, we observed that a subset of animals expressed *eff-1* at high levels, 30-50 molecules (Fig. 2b,c). Interestingly, similar high levels were seen at the same time in P2.p cells, even though they have already fused to the hyp7 syncytium one larval stage earlier. In addition, we observed that *eff-1* expression remained high in recently fused P3.p cells, as judged on the ruffling or absence of AJM-1, before disappearing by the end of the L2 stage (Supplementary Fig. 2a). To confirm that high *eff-1* expression preceded cell fusion and was not induced by any cell fusion events that happen to rapid to be captured by changes in AJM-1 localization, we examined *eff-1* expression in mutants with a temperature-sensitive loss-of-function point

mutation in *eff-1* (Mohler et al., 2002). Indeed, at the restrictive temperature we still found high levels of *eff-1* mRNA in P3.p, but not P4.p, even as P3.p cell fusion was fully inhibited (Supplemental Fig. 2b).

Although the resulting *eff-1* distribution is bimodal (Fig. 2d), the fraction of P3.p cells expressing high *eff-1* levels was smaller than the observed frequency of cell fusion in this strain (Fig. 1f), indicating that *eff-1* was expressed at high levels for only a short duration before the cell fuses. If bimodal *eff-1* expression is the driver of the stochastic hyp7/fusion versus VPC fate decision, then in mutants where the cell fate frequency is different the height of the two peaks rather than the overall width of *eff-1* distribution would be changed (Fig. 1a). To test this prediction we quantified *eff-1* levels in two genotypes with changed P3.p fusion frequency. First, we used a genotype carrying a functional LIN-39::GFP insertion (*lin-39(++))* with only ~2% P3.p fusion frequency (Fig. 1b). Indeed, we found that the *eff-1* distribution only showed a peak at low *eff-1* levels (Fig. 2e). In contrast, in the *cwn-1(0)* mutant with high (>90%) P3.p fusion, the peak at low *eff-1* was much reduced and instead more animals showed high *eff-1* expression (Fig. 2f), even though the absolute *eff-1* level in these animals was not significantly elevated compared to animals with wild-type fusion frequency (Fig. 2d).

Taken together, these results show that *eff-1* expression is bimodal at the time of the hyp7/fusion versus VPC fate decision, with the amplitude of both peaks in the distribution changing in accordance with the frequency of P3.p hyp7/fusion fate in mutants. This raises the question how bimodal *eff-1* expression is generated and controlled by the upstream signaling network (Fig. 1b). One possibility is that the activity of upstream signaling proteins is already bimodal. Alternatively, the activity of the actors just upstream of *eff-1* might be stochastic but in a graded, continuous manner and bimodality in *eff-1* might generated by interactions between these different layers of the signaling network. To address this question, we next examined variability in known upstream regulators of *eff-1* expression.

Bias of cell fate decision by noise in LIN-39 protein level

The Hox transcription factor LIN-39 inhibits Pn.p hyp7/fusion fate by repressing *eff-1* expression (Shemer and Podbilewicz, 2002), with *lin-39* null mutations causing all Pn.p cells to fuse in the L1 larval stage (Clark et al., 1993; Wang et al., 1993). Hence, stochastic variability in LIN-39 protein levels could be a driver of bimodal *eff-1* expression, with *eff-1* upregulated only in P3.p cells where LIN-39 levels falls below a certain threshold. It was shown previously that LIN-39 levels are similar between P3.p and P4.p in early L2 larval stage animals prior to cell fusion (Pénigault and Félix, 2011a), even though both cells have strikingly different frequency of hyp7/fusion versus VPC fate (Fig. 1f). This indicates that absolute LIN-39 levels are unlikely to explain the difference in cell fate bias between P3.p and P4.p. However, it is possible that the dependence of *eff-1* expression on LIN-39 level differs between P3.p and P4.p and that variability in LIN-39 levels in P3.p between animals is indeed sufficient to explain the outcome of the P3.p cell fate decision. To connect animal-to-animal variability in LIN-39 level with P3.p cell fate, it is essential to monitor LIN-39 dynamics and cell fusion in time in single animals. To achieve this, we performed time-lapse microscopy on animals carrying a *lin-39::GFP*

translational fusion (Sarov et al., 2014) and *ajm-1::GFP* as a cell fusion marker (Supplementary Movies 3-4, Fig. 3a,b). Since *lin-39::GFP (lin-39(++))* is present as a multi-copy insertion, it decreased the P3.p fusion rate from ~30% to ~2%, making it challenging to capture sufficient P3.p fusion events. For that reason, we further crossed these reporters into a *cwn-1(0)* background, elevating P3.p and P4.p fusion rate to 20% and 14%, respectively (Supplementary Table 1).

We observed that LIN-39 was present in the P3.p nucleus at the start of the L2 larval stage and remained there for the entire larval stage when P3.p assumed VPC fate (Fig. 3a). However, in P3.p cells that fused, nuclear LIN-39 levels decreased rapidly as soon as fusion commenced and fully disappeared within 90 mins (Fig.3b), consistent with observations in Ref. (Pénigault and Félix, 2011a). We quantified nuclear LIN-39 dynamics in P3.p in multiple animals (Fig. 3c). On average, LIN-39 levels fell during the early L2 larval stage, reaching a minimum around the time of P3.p fusion even in non-fusing P3.p cells. However, we observed significant variability in LIN-39 levels, both in time and between different animals. To test whether this variability correlated with P3.p cell fate outcome, we compared the distribution of LIN-39 levels, averaged over 3 hrs prior to fusion in P3.p cells, that assumed hyp7/fusion fate with the distribution in P3.p cells that assumed VPC fate for the same time window but now prior to the average time of P3.p fusion measured for this strain (Fig. 3d). We find a strong overlap between the two distributions, even if we increase the time window (Supplementary Fig. 3a) making it unlikely that variability in absolute LIN-39 level is the sole noise source driving bimodal *eff-1* expression and the decision to fuse. These observations were performed in a mutant lacking the Wnt ligand *cwn-1*, but this change in Wnt levels did not impact LIN-39 levels, as LIN-39 dynamics and levels were quantitatively similar in the small number of animals that undergo P3.p fusion with wild-type Wnt (data not shown and consistent with Ref. (Pénigault and Félix, 2011a)).

These results leave open the question whether the observed variability in LIN-39 has any effect on the P3.p cell fate outcome. LIN-39 inhibits *eff-1* expression in parallel with the Wnt signaling pathway (Fig. 1b) and variability in Wnt signaling could instead be the main driver of the P3.p cell fate decision. A mathematical model of this network (Fig. 3e) showed that both when variability in Wnt was the sole driver of the cell fate decision and when variability in Wnt and LIN-39 contributed in equal measure, the distribution of LIN-39 levels between cells that do not fuse and those that do, overlapped substantially (Fig. 3f), similar to our data (Fig. 3d). However, the model predicted that we could differentiate between these two scenarios, by comparing the difference in LIN-39 levels between pairs of cells, where one fuses and one does not: if noise in LIN-39 and Wnt drive the stochastic decision with similar strengths, fusing cells will have lower LIN-39 levels than non-fusing cells, even when based on absolute LIN-39 levels we cannot predict which cell will fuse (Fig. 3g). If only noise in Wnt signaling drives the stochastic decision, then difference in LIN-39 levels will not be predictive of cell fate when comparing pairs of cells (Fig. 3g).

In *lin-39::GFP; cwn-1(0)* animals, not only P3.p but also P4.p assumed hyp7/fusion fate in a stochastic manner, allowing us to test whether differences in LIN-39 levels between P3.p

and P4.p are correlated with their eventual fate. First, we established that in this strain LIN-39 distributions for P3.p and P4.p were similar and also showed substantial overlap between fusing and non-fusing cells (Supplementary Fig. 3b). We then selected animals in which one cell, either P3.p or P4.p, fused but the other assumed VPC fate (Fig. 3h). Indeed, in these animals absolute LIN-39 level was not predictive of the eventual fate of P3.p or P4.p, but we observed a significant correlation between fate and the difference in LIN-39 levels between P3.p and P4.p (Fig. 3i), with fusing cells having lower LIN-39 than their non-fusing neighbor cell (P = <0.01, Fisher's Exact Test). This shows that noise in LIN-39 levels drives the hyp7/fusion versus VPC fate decision, but likely in conjunction with another noise source.

β-catenin activation dynamics during the cell fate decision

To test whether the noise source acting in parallel to noise in LIN-39 levels is found within the Wnt signaling pathway, we quantified activation of the Wnt pathway by monitoring the accumulation dynamics of BAR-1/β-catenin during the stochastic decision, in a strain carrying a functional *bar-1::GFP* reporter (Eisenmann et al., 1998). Upon activation by Wnt ligands, the continual degradation of β-catenin is halted and β-catenin accumulates in the cell and nucleus (Sawa and Korswagen, 2013). In P3.p, the presence of BAR-1 is required to inhibit hyp7/fusion fate and *eff-1* expression, in parallel and in addition to LIN-39 (Eisenmann et al., 1998). In contrast to β-catenins involved in the Wnt asymmetry pathway (Mila et al., 2015; Park and Priess, 2003), dynamics of BAR-1 during canonical Wnt signaling is poorly characterized. Based on previous observations, we expected BAR-1 to show approximately constant levels in P(3-8).p cells, similar to LIN-39. Instead, we found that BAR-1::GFP levels were strikingly dynamic, with no BAR-1::GFP in P(3-8).p at the start of the L2 stage - though some non-Pn.p cells were expressing GFP at this time - followed by strong, coordinated pulse of BAR-1::GFP accumulation in P(3-8).p at the mid-L2 stage that lasted 1-4 hours (Supplementary Movie 5, Fig. 4a-c). The BAR-1::GFP signal was detected both in the nucleus and cytoplasm. Additionally, the P3.p cell, which is thought to be the farthest from the source of Wnt ligands (Harterink et al., 2011; Pénigault and Félix, 2011b), did not always exhibit the lowest BAR-1::GFP levels (Fig. 4c), suggesting that cell-intrinsic factors influence the degree of β-catenin activation in each Pn.p cell. Interestingly, the amplitude of the BAR-1::GFP pulse was variable both between cells (Fig. 4b,c) and when comparing the same cell between different animals (Fig. 4d), as was the time at which BAR-1::GFP began accumulating (Fig. 4d).

In BAR-1::GFP reporter animals, no P(3-8).p cells fused during the L2 stage in 30 animals (Supplementary Table 1), indicating that the fluorescently tagged BAR-1 is functional and gives rise to a BAR-1 overexpression phenotype. To reflect this, we will refer to the BAR-1 reporter strain as *bar-1(++)*. To increase the frequency of hyp7/fusion fate, we used two different approaches. First, we removed the inhibitor LIN-39, using the *lin-39(n709)* temperature sensitive loss-of-function mutant to bypass the requirement for *lin-39* during the L1 larval stage, leading to 16/70 P3.p cells assuming hyp7/fusion fate in *bar-1(++);lin-39(lf)* animals (Supplementary Table 1). We found that *bar-1(++);lin39(lf)* animals showed similar BAR-1::GFP pulses, although with reduced amplitude (Fig. 4e), suggesting that LIN-39 influences Wnt signaling upstream of BAR-1. Next, we sought to lower BAR-1 levels in the *bar-1(++)*

background by decreasing activity of the Wnt signaling pathway, using the *cwn-1(0)* mutation. As expected, in these animals, 4/64 P3.p cells assumed hyp7/fusion fate (Supplementary Table 1) and BAR-1::GFP levels were reduced (Fig. 4f). However, we found that in *bar-1(++);cwn-1(0)* animals, BAR-1::GFP pulses were significantly delayed and occurred later in the larval stage when compared to *bar-1(++)* and *bar-1(++);lin-39(lf)* animals.

Variability in β-catenin pulse dynamics

To characterize variability in BAR-1 accumulation dynamics, we used a simple mathematical model of BAR-1 dynamics to fit to the experimental data (Fig. 5a, see Materials and Methods for details). Briefly, we assume that prior to the BAR-1 pulse, Wnt signaling is inactivated and BAR-1 is degraded. At time t_0, Wnt signaling is activated, leading to inhibition of BAR-1 degradation and hence linear accumulation of BAR-1 in the cell. Linear BAR-1 accumulation continues for a pulse duration T in cells that assume VPC fate or until the time of fusion, t_{fusion}, in cells that assume hyp7/fusion fate. Upon fusion BAR-1 vanishes immediately, whereas in cells that assume VPC fate, BAR-1 levels decrease exponentially once the pulse ends. This simple model fitted the experimental data surprisingly well (Fig. 5a,b). Moreover, it allowed us to describe each BAR-1 pulse by three parameters: pulse onset time t_0, pulse slope s and pulse duration T for VPC cells or fusion time t_{fusion} for hyp7/fusion cells.

We first compared the timing of the onset of BAR-1 accumulation between P3.p and P4.p cells. Both in *bar-1(++)* and *bar-1(++);lin-39(lf)* animals, considerable variability existed in t_0, the time of the onset of the BAR-1 pulse, between these cells, with BAR-1 accumulation in P3.p preceding that in P4.p as often as the reverse (Fig. 5b,c). At the same time, pulse onset was correlated between P3.p and P4.p, meaning that if BAR-1 accumulation started late in the L2 larval stage in P3.p, it was also likely to start late in P4.p (Fig. 5c). Strikingly, we not only found that in the *bar-1(++); cwn-1(0)* mutant the onset of the BAR-1 pulse was delayed, but also that the variability in pulse onset time between P3.p and P4.p was reduced, with the onset of BAR-1 accumulation occurring in P3.p and P4.p within 20 min in all animals (Fig. 5c). This result suggests that the Wnt ligand *cwn-1* not only controls the average onset of BAR-1 pulses, but also induces variability in onset time between P3.p and P4.p.

We also observed a clear variability in the duration of BAR-1 pulses when comparing pulses in the same cell between animals (Fig. 5b,d). We examined whether the onset and the duration of BAR-1 pulses were correlated. Because the duration of the L2 larval stage varied both between strains and between animals in the same strain, we examined the pulse onset time t_0/T_{L2} and duration T/T_{L2} relative to the duration of the larval stage, T_{L2}. In this case, we found a striking anti-correlation, with late pulse onset resulting in shorter pulses (Fig. 5d). In fact, the data for all strains clustered along the line $T/T_{\mathrm{L2}} = 0.66 - t_0/T_{\mathrm{L2}}$, consistent with a model in which the end of the BAR-1 accumulation occurs at 66% of the L2 larval stage independent of the BAR-1 pulse onset time. Strikingly, this correlation also held for the *bar-1(++); cwn-1(0)* mutant, where not only the onset of BAR-1 pulses was delayed but also the L2 larval stage was much extended, lasting up to 22 hrs compared to ~12 hrs for wild-type animals. This also

means that Wnt signaling, in contrast to the pulse onset, likely plays no role in determining the end of the pulse.

Giving the observed qualitative difference in the degree of variability of the start and the end time of BAR-1 pulses, we next asked whether the time of fusion correlated most strongly with the start or the end of the pulse. In the first case, it would mean that the time of fusion would show strong variability with respect to both the start of the L2 larval stage and the end of the pulse, whereas in the latter case it would mean that fusion would occur at a fixed fraction of the larval stage duration. We tested this in *bar-1(++);lin-39(lf)* animals, where the largest fraction of Pn.p cells, typically P3.p, assume hyp7/fusion fate. However, because the amplitude of the BAR-1 pulses in P3.p is often low (Fig. 4e), making it challenging to accurately determine the pulse onset time t_0, we compared within the same animal the fusion time t_{fusion} in P3.p cells that assume hyp7/fusion fate with either the pulse onset time t_0 or pulse end time $t_0 + T$ in P4.p cells that assume VPC fate (Fig. 4a,e, Supplementary Fig. 5a). Strikingly, we find that the time of fusion is more strongly correlated with the pulse onset time (R=0.86) than with the pulse end time. In particular, the data clustered tightly along the line $t_{\mathrm{fusion}}/T_{\mathrm{L2}} = 0.2 + t_0/T_{\mathrm{L2}}$, suggesting that cell fusion occurs at a time $0.2T_{\mathrm{L2}}$, or on average ~2 hrs, after the onset of the BAR-1 pulse. Together, these results suggest a model in which the timing of pulse onset and cell fusion are co-regulated, independently of timing of the BAR-1 pulse end and in a manner that is highly variable between animals.

Finally, we compared the distribution of the onset time t_0 and linear slope s of BAR-1 accumulation pulses between strains. We found that not only t_0 but also pulse slope s were highly variable between animals in all strains (Fig. 5f,g). We found that the pulse parameters of *bar-1(++)* and *bar-1(++);lin-39(lf)* were similar, although we did observe more pulses with low slope in *bar-1(++);lin-39(lf)*, consistent with the assumption that difference in hyp7/fusion fate frequency is largely due to absence of the fusion inhibitor LIN-39. We assumed that the increase in frequency of hyp7/fusion fate in *bar-1(++);cwn-1(0)* animals was due to a decrease in BAR-1 level. In the context of the observed BAR-1 pulses this could be achieved in two independent ways, either by decreasing the slope s or by delaying the onset time t_0 of the BAR-1 pulse (Fig. 6a,b). Given that BAR-1 accumulation is thought to be proportional to the amount of external Wnt ligands, we expected the *cwn-1(0)* mutant to predominantly lead to a decrease in the rate of BAR-1 accumulation. Surprisingly, we found that the pulse slope distribution was highly similar for *bar-1(++)* and *bar-1(++);cwn-1(0)* animals (Fig. 5f) and that the only different pulse characteristic was the delayed pulse onset (Fig. 5g).

Bias of cell fate decision by variability in β-catenin pulse timing

To understand how variability in BAR-1 pulse dynamics influences hyp7/fusion versus VPC fate decision, we extended our mathematical model of the cell fate induction network to include BAR-1 pulses (Fig. 6a). Specifically, we assumed that at time t_0 the level of inhibition by Wnt signaling, $c_w(t)$, increases with linear slope s, with stochastic variability in both variables. Currently, factors that induce *eff-1* expression or hyp7/fusion fate are not known. However, our observations suggest that induction of hyp7/fusion cell fate must also be under temporal control.

First, cell fusion does not occur earlier in development, even though the inhibitor BAR-1 is not present (Fig. 5a). Moreover, the time of fusion is itself variable but correlated with the start of the BAR-1 pulse (Fig. 5e). In the model, we therefore assume that a signal to activate *eff-1* expression is present from time t_{fusion} with level c_a, again with stochastic variability in both variables. Fusion occurs when at time t_{fusion} the inhibitory Wnt signal c_w is sufficiently low that the *eff-1* level $e(t)$ is above the threshold e_{th} required to induce fusion. In the model, this can be achieved both by stochastic variability in pulse slope and pulse onset timing (Fig. 6b). In general, this extended model reproduces the experimentally observed characteristic of BAR-1 pulse timing (Supplementary Fig. 6a).

The model can explain the increased frequency of hyp7/fusion in *bar-1(++); lin-39(lf)* and *bar-1(++); cwn-1(0)* animals. First, the decrease of *eff-1* inhibition by the absence of LIN-39 in the *lin-39(lf)* background increases the range of activating and inhibitory signals c_a and c_w for which *eff-1* is expressed above the threshold e_{th}, so that a higher fraction of the animals with elevated BAR-1 levels in the *bar-1(++)* background still result in fusion (Fig. 6c). In contrast, for the *bar-1(++); cwn-1(0)* mutant, the observed delay in pulse onset causes lower inhibitory Wnt signals c_w at the time of fusion, leading to more frequent fusion events. Specifically, in many animals the onset of the BAR-1 pulse occurs after expression of *eff-1* is induced by the activator, i.e. c_w=0 at the time of fusion.

Next, we used experimentally testable predictions to establish the relative importance of variability in BAR-1 pulse timing and pulse slope in biasing the hyp7/fusion versus VPC fate decision. First, the model predicted that when compared at the time when cell fusion is activated, BAR-1 levels in cells that assume hyp7/fusion fate should be lower than in cells that assume VPC fate (Supplementary Fig 6b). However, because we cannot infer the time of activation of cell fusion in cells that do not fuse but instead assume VPC fate, we could not test this experimentally. However, the model predicted that, if variability in pulse timing was more important for determining BAR-1 levels than variability in pulse slope, cells that fuse cannot be distinguished from those that assume VPC fate based on BAR-1 pulse slope (Fig. 6d), but that fusing cells do have a delayed pulse onset time t_0 compared to non-fusing cells (Fig. 6f). In contrast, when variability in pulse slope dominates BAR-1 levels, then fusing and non-fusing cells differ in slope rather than pulse onset time (Supplementary Fig. 6c). To test this prediction, we first compared pulse slope and pulse onset time between P3.p and P.4p cells in *bar-1(++)* animals, where these cells never assume hyp7/fusion fate. We found that the distributions $P(s_{\mathrm{P4.p}}\text{-}s_{\mathrm{P3.p}})$, of difference in pulse slope, and $P(t_{0,\mathrm{P4.p}}\text{-}t_{0,\mathrm{P3.p}})$, of difference in pulse onset time, were symmetrical, i.e. showed no systematic difference between P3.p and P4.p (Fig. 6e,g). We then examined the difference in pulse slope and onset time in *bar-1(++); lin-39(lf)* animals, comparing animals where P3.p fused but P4.p assumed VPC fate with animals where both P3.p and P4.p assumed VPC fate. We found no bias towards lower pulse slope in fusing P3.p cells compared to non-fusing P4.p cells (Fig. 6e, blue line), but instead found a distribution very similar to that observed in *bar-1(++)* animals. However, we found that BAR-1 pulse onset in fusing P3.p cells was delayed compared to non-fusing P4.p cells (Fig 6g, blue line), with only one animal with a fusing P3.p cell showing BAR-1 accumulation in P3.p prior to P4.p. This difference was particularly striking compared to the *bar-1(++)* strain, which otherwise showed no

difference in relative timing of BAR-1 pulse onset between P3.p and P4.p relative to *bar-1(++);lin-39(lf)* animals (Fig. 5c).

Even though the above results indicated that BAR-1 pulse timing biased the hyp7/fusion versus VPC fate decision, it left open whether variations in pulse timing achieve this by specifically modulating BAR-1 levels at the time the decision to fuse or not is made. We previously found that the only difference in BAR-1 pulse dynamics between *bar-1(++)* and *bar-1(++);cwn-1(0)* animals was the delayed onset of BAR-1 pulses (Fig. 5g), additional evidence that pulse timing affects cell fate frequency. Indeed, the model showed the delayed onset of BAR-1 pulses increased the frequency of hyp7/fusion fate by lowering BAR-1 levels at the time when *eff-1* expression and cell fusion is activated (Fig. 6a,b). Moreover, the model predicted that fusing cells in *bar-1(++);cwn-1(0)* mutants should have lower BAR-1 levels than fusing cells in *bar-1(++);lin-39(lf)* mutants, where fusion frequency is instead increased by removing the inhibitor LIN-39 (Fig. 6h). Indeed, when we compared BAR-1::GFP fluorescence at the time of cell fusion in *bar-1(++);lin-39(lf)* and *bar-1(++);cwn-1(0)* animals, we found a bias towards lower BAR-1 levels in fusing P3.p and P4.p cells in the *cwn-1(0)* background. This provides further evidence that delayed BAR-1 pulse timing influences the cell fate decision by reducing the inhibitory BAR-1 levels at the time the decision is made. To further link BAR-1 levels to inhibition of cell fusion, we quantified *eff-1* transcripts in *bar-1::gfp* animals and indeed found a negative correlation: Pn.p cells with visible BAR-1::GFP had few *eff-1* transcripts, while unfused Pn.p cells without BAR-1::GFP showed low and high *eff-1* levels (Supplemental Figure 6d). Together, these results show that variability in the timing of BAR-1 accumulation pulses are a key noise source biasing the hyp7/fusion versus VPC fate decision.

Discussion

Emerging picture of the network

Here we describe a cell-autonomous stochastic cell fate decision using time-lapse microscopy and modeling of the components of the network. The bimodality we expected to find in the network was at the level of *eff-1* transcription, the most downstream element in the network and necessary and sufficient to initiate the hyp7/fusion fate. Mutants that change the fate frequency increase or decrease the fraction of animals with high *eff-1* expression, but the shape of the *eff-1* distribution remains unchanged (Figure 2d,e,f), suggesting that the expression of *eff-1* is triggered by the activity (or lack thereof) of other factors upstream in the genetic network. We then characterized two potential noise sources upstream of *eff-1* expression that biased the stochastic cell fate decision. We found continuous variability in the levels of LIN-39 and pulse dynamics in BAR-1 tightly associated with the fate decision. Both factors biased the cell fate decision by ultimately reduced levels biasing the hyp7/fusion fate, but achieved this by distinct mechanisms: first, variability in the relative levels of LIN-39, and second, by variability in the timing of the BAR-1 pulses in response to Wnt ligands. The combined effect of two inhibitors creates a distribution of inhibitory variability that is opposed by the activity of a presumed positive regulator of *eff-1.* Currently, it is still unclear what transcription factor(s) are primarily responsible for the activation of *eff-1*, but our data suggests the presence of one due to the fact that in the absence of any BAR-1 pulses, the *eff-1* gene still is expressed at a particular point in time. Indeed, most mutations that alter the frequency of the P3.p hyp7/fusion cell fate lie in proteins that act as inhibitors to the cell fusion process (Alper and Kenyon, 2001, 2002; Gorrepati et al., 2013; Koh et al., 2002; Smurova and Podbilewicz, 2016). Fewer mutations have been found that decrease cell fusion rates. However, previous studies have shown *lin-22* loss-of-function mutations decreased P3.p cell fusion frequencies (Katsanos et al., 2017; Schlager et al., 2006). LIN-22 codes for a Hairy/Enhancer of Split-related transcription factor, which was found to act in the Wnt pathway by repressing *egl-18*, a GATA transcription factor, a repressor of cell fusion in the seam cells (Gorrepati et al., 2013; Katsanos et al., 2017; Wrischnik and Kenyon, 1997). Therefore, variations in not only the inhibitor molecules, but LIN-22 could create noise and variability that leads to stochastic *eff-1* expression and cell fusion. Additionally, the classB *synMuv* gene class has also shown to decrease cell fusion frequencies, likely by affecting general transcription characteristics (Chen and Han, 2001).

Experiments reveal intricate timing program

The regulation of the timing of cellular and developmental events has not been widely studied in *C. elegans,* besides the discovery of heterochronic mutants that completely lack or repeat larval stages and their associated developmental events (Ambros and Horvitz, 1984). Using our time-lapse approach, we could investigate the temporal progression and timing of a cell fate decision in a multicellular animal. Using the molting cycle as developmental reference points, we found that the timing of the cell fusion event was surprisingly regulated and conserved, even in mutants that had high cell fusion frequencies. In addition to the tight temporal control of cell fusion, we also saw a significant correlation in the onset of the BAR-1

pulse among Pn.p cells in the same animal, suggesting that the BAR-1 pulse is globally regulated and directly linked to the cell fusion event (Fig 5c). Similarly, while the onset of the pulse varied from animal-to-animal, the end of the pulse appears more tightly linked to the molting cycle, as it occurs at a fixed fraction of the larval stage duration. Negative feedback of the Wnt/β-catenin pathway has been shown to occur through the regulator Axin (Jho et al., 2002). However, this implies that the end of the pulse would not be tightly linked to a fixed point in the larval stage, suggesting that negative feedback does not play a role in this β-catenin signaling event (Fig 5d).

Unexpected dynamics of β-catenin signaling

For the first time we followed β-catenin dynamics during *C. elegans* development, and in particular, a specific cell fate decision, and detected pulses of β-catenin in the cells that coincided with a cell-fate decision. Genuine pulses of β-catenin signaling have only been directly observed in single isolated cells, immediately after exposure to Wnt ligands in the medium (Kafri et al., 2016). These response were variable from cell-to-cell and showed pulsing dynamics on time-scales similar to the BAR-1 dynamics *in vivo*. In our study, it is still an open question how a concerted response to Wnts at a particular time of development is established, especially since Wnt ligands are already present in the worm at this time. This suggests that cell autonomous factors, such as changes to the degradation complex, or the expression or regulation of Wnt receptor could be changing the cells exposure or sensitivity to Wnt ligands. Such a mechanism was also seen in *C. elegans* neuroblasts, where the cells modulate Wnt signaling by dynamically expressing Wnt receptors (Mentink et al., 2014). *C. elegans* contains multiple Wnt ligands. Unexpectedly, with the removal of *cwn-1*, we saw that the accumulation rate was unchanged but rather the timing of the pulse was delayed. Due to the fact that BAR-1 shuts off at a fixed time-point during development, this effectively reduced in the duration of BAR-1 accumulation, resulting in lower levels of BAR-1 in these mutants. This was unexpected considering the current model of Wnt signaling, where levels of Wnt ligand directly translate into the degree of relaxation from the degradation complex, and Wnt levels would have no effect on the time at which the cell begins to accumulate BAR-1. Particularly striking is that loss of *cwn-1* also decreased the variability in timing between the Pn.p cells in their temporal response. One source of *cwn-1* is from the sex myoblast, located near the P6.p cell in the midbody of the animal. Variability in the transcription of this gene or delivery of the Wnt molecules from this cell could provide a significant source of noise, whereas other sources of Wnt ligands could be less noisy.

In most animal models, cell fate decisions and differentiation takes place over the time-scale of days and their transitions are much more gradual and continuous, making the link between specific molecular events and eventual cell fate outcomes much more difficult to describe or detect, therefore, information is lacking tying the exact molecular details of the dynamics or activity of β-catenin and its role in cell fate choices. Additionally, attempts to determine the temporal requirements of the Wnt pathway are rather crude and on the time-scales of days, not minutes, making it unclear whether β-catenin signaling normally occurs in pulses or is instead activated over longer periods of time. While pulses of β-catenin in multicellular animals have not been directly observed except in this study, likely due to technical

limitations in the imaging over long time periods, there is some evidence suggesting that the β-catenin pathway acts in pulses in other developmental cell fate decisions. For example, after muscle injury, the Wnt pathway becomes active in myoblasts as they start to regenerate muscle over a time-scale of days. A quarter of myoblasts were found to express β-catenin the first day after injury, which disappeared after the third day, suggesting that β-catenin was transiently expressed (Murphy et al., 2014). Additionally, after the transient expression, downregulation of β-catenin was required for the normal myoblast response, suggesting that prolonged periods of activation, suggesting a pulse model of regulation. Additionally, Wnt/β-catenin signaling was shown to act bi-phasically in the specification of cardiac cells in Zebrafish, with β-catenin positively regulating cardiac differentiation early in development, while later, β-catenin negatively regulating differentiation, suggesting that each requirement of Wnt signaling could represent a separate pulse (Ueno et al., 2007). However, directly linking the dynamics of β-catenin signaling and these cell fate decisions appears unresolved.

C. elegans contains multiple Wnt ligands. With the removal of *cwn-1*, we saw that the accumulation rate was unchanged but rather the timing of the pulse was delayed. Due to the fact that BAR-1 shuts off at a fixed time-point during development, this created a reduction in the duration of BAR-1 accumulation, resulting in lower levels of BAR-1 in these mutants. This was unexpected considering the current model of Wnt signaling, where levels of Wnt ligand directly translate into the degree of relaxation from the degradation complex, and Wnt levels would have no effect on the time at which the cell begins to accumulate BAR-1.

The Wnt/β-catenin pathway has been intensively studied in *C. elegans*, with a significant focus on Wnt-guided cell migration and the SYS-1/POP-1 Wnt asymmetry pathway, required for proper fate of seam cells and some neurons, while the role of BAR-1 in the Pn.p cells has remained less characterized (Mila et al., 2015; Park and Priess, 2003). β-catenin/BAR-1 is conventionally known to act as a transcriptional co-activator with the TCF/POP-1 protein, suggesting that the effect BAR-1 has on *eff-1* is through another intermediate protein. Some descriptions of the pathway have attempted to identify the molecular targets of BAR-1 using RNA-sequencing in a *bar-1* mutant (Van Der Bent et al., 2014). However, the specific changes in the Pn.p cells that would be relevant to the stochastic cell fate decision would be difficult to detect in bulk tissue experiments of whole animals.

Control of cell fate frequency

To observe the localization and protein levels of LIN-39 and BAR-1, we expressed extragenic copies of proteins fused with a fluorescent markers. For both proteins, this also was associated with an overexpression phenotype, since additional copies of the protein changed the rate of P3.p cell fusions. This reduction in the P3.p fusion rate prevented the analysis or observation of hyp7/fusion fated cells in an otherwise normal genetic background. To circumvent this problem, we sensitized the genetic background using Wnt or *lin-39* mutations. With these changes, we were far from normal gene expression levels in wild-type *C. elegans*, but could exploit the situation in order to determine the principles of the stochastic decision.

In summary, we propose that the balance of inhibitors and activators at a critical time point is integrated into the promotor of the *eff-1*, which then either triggers expression or keeps

the gene inactive. We showed that timing of the pulse is a source of variability to bias the decision. Could this be a real mechanism to control a cell fate decision, or to control cell fate frequencies? Theory suggests that the relative timing of factors could be a plausible way to regulate genes, especially when cooperativity between multiple factors or transcription factors is taken into account (Levine et al., 2013). Our research shows multiple noise sources (Hox gene levels, BAR-1 level and pulse timing, the dynamics of an activator) can be tuned to change frequency of hyp7 fate. Additionally, it will be interesting to see whether change in fate frequency in other isolates can be traced back to variation in these sources, particularly changes in timing BAR-1 pulse.

Materials and Methods

CONTACT FOR REAGENT AND RESOURCE SHARING

Further information and requests for resources and reagents should be directed to and will be fulfilled by the Lead Contact, Jeroen van Zon (j.v.zon@amolf.nl).

EXPERIMENTAL MODEL DETAILS

Strains

All strains were handled according to the standard protocol on Nematode growth medium (NGM) agar plates with OP50 bacteria (Brenner, 1974). Experiments were performed on L2 stage hermaphrodites. Strains were obtained from the CGC unless otherwise indicated. The following mutations were used in this study: LGII: *cwn-1(ok546),* LGIII*: lin-39(gk893), lin-39(n709)*, *unc-119(ed3),* LGIV: *unc-30(e191),* and LGX: *bar-1(ga80).* The following transgenes were used in this study: *ncIs13[ajm-1::GFP], sIs11337[rCesY37A1B.5::GFP + pCeh361)], ouIs20 [ajm-1::mCherry + unc-119+], itIs37[pie-1p::mCherry::H2B::pie-1 3'UTR + unc-119(+)] IV, stIs10116[his-72(promoter)::his-24::mCherry::let-858 3'UTR + unc-119(+)], stIs10311[lin-39::TGF(3D3)::GFP::TY1::3xFLAG]*, *gaIs45[pDE218(bar-1::bar-1::GFP)]* (Eisenmann et al., 1998), and *stIs10226[his-72p::HIS-24::mCherry::let-858 3' UTR + unc-119(+)]*. The presence of the *cwn-1(ok546)* homozygous deletion was confirmed by nested PCR screening. The following primers were used: outer left ('5-TCGTTTCTGACATGGCTCAC-3'), outer right ('5-ACCCATCCTTTCCCAATCTC-3'), inner left ('5-CGTATCCACGACCACAACAG-3') and inner right (5'-AGAATCTTCACACCAACGGG-3').

METHOD DETAILS

Time-lapse imaging

The microchamber size used in the study was 190 µm x 190 µm, with a depth of 10 µm and made as previously described and imaged with a custom time-lapse microscope (Gritti et al., 2016). Using an eyelash attached to a glass pipette, bacteria was used as "glue" to transfer eggs into the microchambers. A Nikon Ti-E inverted microscope with a large chip camera (Hamamatsu sCMOS Orca v2) and a 60 X magnification objective (NA=1.4 oil immersion) was used. Transmission imaging was performed using an LED light source (CoolLED pE-100 615nm), while 488 and 561 nm fluorescence images were acquired using Coherent OBIS LS 488-100 and OBIS LS 561-100 lasers, respectively. Images were acquired in a temperature controlled room at 19° with a sample temperature of 22°. Exposure time was 10 ms and approximately 25 images were taken with a z-distance of 1 µm. Images were taken every 20 min. Images were 2048 x 2048 pixels and saved in 16-bit TIFF format.

Quantitative Image Analysis

For all experiments, transmitted light images where used to identify molt times. ImageJ and visual inspection of cell fusion markers (depending on genotype) were used to score cell fusion events. Custom Python scripts and ImageJ were used to quantitatively analyze the acquired images. In general, images to be used for quantitative analysis were first corrected for uneven laser illumination by a normalization procedure to correct for position-specific differences in laser intensity. The normalization procedure was carried out by dividing each pixel

intensity value by the flat field pixel intensity, normalized to the median value of the flat field image. This process was required since the laser light intensity is reduced at the side of the chambers compared to center, thus the normalization procedure corrects for any postion-dependent laser intensity variability. The region of interest was cropped at this time. Pn.p cells were manually identified by stereotyped nuclear position location and the domains of *ajm-1::gfp/mcherry* expression, if present. To measure *lin-39::gfp* expression, a mask was manually drawn around the nucleus and the mean fluorescence intensity of the pixels within the mask was calculated. The z-stack image closest to the center of the nucleus was used, which was the most in focus. A background fluorescence measurement for each image was obtained by creating a mask of the intranuclear space in a region near P3.p and P4.p along the axis of the ventral nerve cord. The background measurement was then subtracted from the mean fluorescence mask for the same image, which corrected image to image variability in the light intensity and animal position. To measure *bar-1::gfp* expression, a mask was manually drawn around the Pn.p cytoplasmic region using *ajm-1::mCherry* signal as a positional guide, with background corrections performed similarly as described above.

Single-molecule fluorescence in situ hybridization (smFISH)

Probe design and smFISH hybridization to visualize *eff-1* mRNA transcripts were performed as previously described (Huelsz-Prince and van Zon, 2017; Raj et al., 2008). Custom probes were designed against the exons of the *eff-1* gene by utilizing the Stellaris® RNA FISH Probe Designer (Biosearch Technologies, Inc., Petaluma, CA). The probes were hybridized with the Cy5 dye (Huelsz-Prince and van Zon, 2017). The sequences of the oligonucleotide probes used in this study are listed in Table 1 of the Supplementary Methods. Animals were collected by washing plates with M9 and were fixed in 4% formaldehyde in 1 X PBS for 45 min at room temperature. Fixed animals were permeabilized in 70% ethanol at least one night at 4°. Subsequently, animals were incubated with the 0.5 µl probes overnight at 30° in Stellaris® Hybridization Solution containing 10% formamide. The next day, animals were quickly washed two times with 10% formamide and 2 X SSC, followed by an incubation wash for 30 min at 30°. DAPI was added at 0.01 µg/ml in a final incubation step for 20 min at 30° C. Animals were mounted in Glox Buffer with catalase and glucose oxidase, and images were acquired with a Nikon Ti-E inverted fluorescence microscope, equipped with a 100X plan-apochromat oil-immersion objective and an Andor Ikon-M CCD camera controlled by µManager software (Edelstein et al., 2014). Stacks of each animal were taken with a z-distance of 0.33 µm and approximately 30 images were taken per animal. Cy5 exposure time was 3 s, while DAPI and GFP exposure time were 100 ms and 500 ms, respectively. Animals were then imaged at 40 X to determine their body length, which was measured using ImageJ by drawing a spline from the tip of the head to the end of the tail. smFISH images were analyzed with a custom Python script using techniques previously described (Raj et al., 2008). The *ajm-1::gfp* transgene was used to determine the cell fusion status.

Modeling

Details of the models are available in Supplementary Methods.

Acknowledgements

We thank Yvonne Goos and Joleen Traets for the coupling the *eff-1* primers to Cy5, and Yvonne Goos for minor technical assistance. This work is part of the research program of the Netherlands Organisation for Scientific Research (NWO) and was performed at the research institute AMOLF. Some *C. elegans* strains were provided by the CGC, which is funded by NIH Office of Research Infrastructure Programs (P40 OD010440). The work was supported by a European Research Council Starting Grant (338200-STOCHCELLFATE) awarded to J.S.v.Z.

Author Contributions

Conceptualization, J.S.v.Z.; Methodology, J.R.K. and J.S.v.Z.; Formal Analysis: J.R.K., J.T, and J.S.v.Z.; Investigation, J.R.K., and J.T.; Writing – Original Draft, J.R.K. and J.S.v.Z.; Writing – Review & Editing, J.R.K. and J.S.v.Z.; Funding Acquisition, J.S.v.Z.; Supervision, J.S.v.Z.

Declaration of Interests

The authors declare no competing interests.

References

Alper, S., and Kenyon, C. (2001). REF-1, a protein with two bHLH domains, alters the pattern of cell fusion in C. elegans by regulating Hox protein activity. Development *128*, 1793–1804.

Alper, S., and Kenyon, C. (2002). The zinc finger protein REF-2 functions with the Hox genes to inhibit cell fusion in the ventral epidermis of C. elegans. Development *129*, 3335–3348.

Ambros, V., and Horvitz, H. (1984). Heterochronic mutants of the nematode Caenorhabditis elegans. Science . *226*, 409–416.

Balaban, N.Q. (2004). Bacterial Persistence as a Phenotypic Switch. Science . *305*, 1622–1625.

Van Der Bent, M.L., Sterken, M.G., Volkers, R.J.M., Riksen, J.A.G., Schmid, T., Hajnal, A., Kammenga, J.E., and Snoek, L.B. (2014). Loss-of-function of β-catenin bar-1 slows development and activates the Wnt pathway in Caenorhabditis elegans. Sci. Rep. *4*, 1–6.

Brabin, C., Appleford, P.J., and Woollard, A. (2011). The Caenorhabditis elegans GATA Factor ELT-1 Works through the Cell Proliferation Regulator BRO-1 and the Fusogen EFF-1 to Maintain the Seam Stem-Like Fate. PLoS Genet. *7*, e1002200.

Brenner, S. (1974). THE GENETICS OF CAENORHABDITIS ELEGANS. Genetics *77*, 71–94.

Chen, Z., and Han, M. (2001). C. elegans Rb NuRD and Ras regulate lin-39-mediated cell fusion during vulval fate specification. Curr. Biol. *11*, 1874–1879.

Clark, S.G., Chisholm, A.D., and Horvitz, H.R. (1993). Control of cell fates in the central body region of C. elegans by the homeobox gene lin-39. Cell *74*, 43–55.

Dietrich, J.-E., and Hiiragi, T. (2007). Stochastic patterning in the mouse pre-implantation embryo. Development *134*, 4219–4231.

Edelstein, A.D., Tsuchida, M.A., Amodaj, N., Pinkard, H., Vale, R.D., and Stuurman, N. (2014). Advanced methods of microscope control using μManager software. J. Biol. Methods *1*, 10.

Eisenmann, D.M., Maloof, J.N., Simske, J.S., Kenyon, C., and Kim, S.K. (1998). The beta-catenin homolog BAR-1 and LET-60 Ras coordinately regulate the Hox gene lin-39 during Caenorhabditis elegans vulval development. Development *125*, 3667–3680.

Félix, M.A. (2012). Caenorhabditis elegans vulval cell fate patterning. Phys. Biol. *9*.

Gamba, P., Jonker, M.J., and Hamoen, L.W. (2015). A Novel Feedback Loop That Controls Bimodal Expression of Genetic Competence. PLoS Genet. *11*, 1–32.

Gleason, J.E., Korswagen, H.C., and Eisenmann, D.M. (2002). Activation of Wnt signaling bypasses the requirement for RTK/Ras signaling during C. elegans vulval induction. Genes Dev. *16*, 1281–1290.

Gorrepati, L., Thompson, K.W., and Eisenmann, D.M. (2013). C. elegans GATA factors EGL-18 and ELT-6 function downstream of Wnt signaling to maintain the progenitor fate during larval asymmetric divisions of the seam cells. Development *140*, 2093–2102.

Gritti, N., Kienle, S., Filina, O., and van Zon, J.S. (2016). Long-term time-lapse microscopy of C. elegans post-embryonic development. Nat. Commun. *7*, 12500.

Gupta, B.P., Hanna-Rose, W., and Sternberg, P.W. (2012). Morphogenesis of the vulva and the vulval-uterine connection*. WormBook 1–17.

Harterink, M., Kim, D.H., Middelkoop, T.C., Doan, T.D., van Oudenaarden, A., and Korswagen, H.C. (2011). Neuroblast migration along the anteroposterior axis of C. elegans is controlled by opposing gradients of Wnts and a secreted Frizzled-related protein. Development *138*, 2915–2924.

Hill, R.J., and Sternberg, P.W. (1993). Cell fate patterning during C. elegans vulval development. Development *18*, 9–18.

Hirabayashi, Y. (2004). The Wnt/β-catenin pathway directs neuronal differentiation of cortical neural precursor cells. Development *131*, 2791–2801.

Hudson, C., Kawai, N., Negishi, T., and Yasuo, H. (2013). B-Catenin-Driven Binary Fate Specification

Segregates Germ Layers in Ascidian Embryos. Curr. Biol. *23*, 491–495.

Huelsz-Prince, G., and van Zon, J.S. (2017). Canalization of C. elegans Vulva Induction against Anatomical Variability. Cell Syst. *4*, 219–230.e6.

Jho, E., Zhang, T., Domon, C., Joo, C., Freund, J., and Costantini, F. (2002). Wnt/β -Catenin/Tcf Signaling Induces the Transcription of Axin2, a Negative Regulator of the Signaling Pathway. Mol. Cell. Biol. *22*, 1172–1183.

Kafri, P., Hasenson, S.E., Kanter, I., Sheinberger, J., Kinor, N., Yunger, S., and Shav-Tal, Y. (2016). Quantifying β-catenin subcellular dynamics and cyclin D1 mRNA transcription during Wnt signaling in single living cells. Elife *5*.

Katsanos, D., Koneru, S.L., Mestek Boukhibar, L., Gritti, N., Ghose, R., Appleford, P.J., Doitsidou, M., Woollard, A., van Zon, J.S., Poole, R.J., et al. (2017). Stochastic loss and gain of symmetric divisions in the C. elegans epidermis perturbs robustness of stem cell number.

Kaufmann, B.B., Yang, Q., Mettetal, J.T., and Van Oudenaarden, A. (2007). Heritable stochastic switching revealed by single-cell genealogy. PLoS Biol. *5*, 1973–1980.

Koh, K., Peyrot, S.M., Wood, C.G., Wagmaister, J.A., Maduro, M.F., Eisenmann, D.M., and Rothman, J.H. (2002). Cell fates and fusion in the C. elegans vulval primordium are regulated by the EGL-18 and ELT-6 GATA factors -- apparent direct targets of the LIN-39 Hox protein. Development *129*, 5171–5180.

Korswagen, H.C. (2002). Canonical and non-canonical Wnt signaling pathways in Caenorhabditis elegans: Variations on a common signaling theme. BioEssays *24*, 801–810.

Korswagen, H.C., Herman, M. a, and Clevers, H.C. (2000). Distinct beta-catenins mediate adhesion and signalling functions in C. elegans. Nature *406*, 527–532.

Levine, J.H., Lin, Y., and Elowitz, M.B. (2013). Functional Roles of Pulsing. Science . *342*, 1193–1200.

Lindström, N.O., Lawrence, M.L., Burn, S.F., Johansson, J.A., Bakker, E.R.M., Ridgway, R.A., Chang, C.H., Karolak, M.J., Oxburgh, L., Headon, D.J., et al. (2014). Integrated β-catenin, BMP, PTEN, and Notch signalling patterns the nephron. Elife *3*, e04000.

Losick, R., and Desplan, C. (2008). Stochasticity and Cell Fate. Science . *320*, 65–68.

Maamar, H., Raj, A., and Dubnau, D. (2007). Noise in Gene Expression Determines Cell Fate in Bacillus subtilis. Science . *317*, 526–529.

Maloof, J.N., and Kenyon, C. (1998). The Hox gene lin-39 is required during C. elegans vulval induction to select the outcome of Ras signaling. Development *125*, 181–190.

Mentink, R.A., Middelkoop, T.C., Rella, L., Ji, N., Tang, C.Y., Betist, M.C., van Oudenaarden, A., and Korswagen, H.C. (2014). Cell intrinsic modulation of Wnt signaling controls neuroblast migration in C. elegans. Dev. Cell *31*, 188–201.

Mila, D., Calderon, A., Baldwin, A.T., Moore, K.M., Watson, M., Phillips, B.T., and Putzke, A.P. (2015). Asymmetric Wnt Pathway Signaling Facilitates Stem Cell-Like Divisions via the Nonreceptor Tyrosine Kinase FRK-1 in Caenorhabditis elegans. *201*, 1047–1060.

Mohler, W. a, Shemer, G., del Campo, J.J., Valansi, C., Opoku-Serebuoh, E., Scranton, V., Assaf, N., White, J.G., and Podbilewicz, B. (2002). The type I membrane protein EFF-1 is essential for developmental cell fusion. Dev. Cell *2*, 355–362.

Mucenski, M.L., Wert, S.E., Nation, J.M., Loudy, D.E., Huelsken, J., Birchmeier, W., Morrisey, E.E., and Whitsett, J.A. (2003). β-Catenin Is Required for Specification of Proximal/Distal Cell Fate During Lung Morphogenesis. J. Biol. Chem. *278*, 40231–40238.

Murphy, M.M., Keefe, A.C., Lawson, J.A., Flygare, S.D., Yandell, M., and Kardon, G. (2014). Transiently active wnt/β-catenin signaling is not required but must be silenced for stem cell function during muscle regeneration. Stem Cell Reports *3*, 475–488.

Myers, T.R., and Greenwald, I. (2007). Wnt signal from multiple tissues and lin-3/EGF signal from the gonad maintain vulval precursor cell competence in Caenorhabditis elegans. Proc. Natl. Acad. Sci. U. S. A. *104*, 20368–20373.

Ohyama, T. (2006). Wnt signals mediate a fate decision between otic placode and epidermis. Development *133*, 865–875.

Park, F.D., and Priess, J.R. (2003). Establishment of POP-1 asymmetry in early C. elegans embryos. Development *130*, 3547–3556.

Pénigault, J.B., and Félix, M.A. (2011a). Evolution of a system sensitive to stochastic noise: P3.p cell fate in Caenorhabditis. Dev. Biol. *357*, 419–427.

Pénigault, J.B., and Félix, M.A. (2011b). High sensitivity of C. elegans vulval precursor cells to the dose of posterior Wnts. Dev. Biol. *357*, 428–438.

Podbilewicz, B., Leikina, E., Sapir, A., Valansi, C., Suissa, M., Shemer, G., and Chernomordik, L. V. (2006). The C. elegans Developmental Fusogen EFF-1 Mediates Homotypic Fusion in Heterologous Cells and In Vivo. Dev. Cell *11*, 471–481.

Raj, A., van den Bogaard, P., Rifkin, S.A., van Oudenaarden, A., and Tyagi, S. (2008). Imaging individual mRNA molecules using multiple singly labeled probes. Nat. Methods *5*, 877–879.

Roiz, D., Escobar-Restrepo, J.M., Leu, P., and Hajnal, A. (2016). The C. elegans hox gene lin-39 controls cell cycle progression during vulval development. Dev. Biol. *418*, 124–134.

Roorda, A., and Williams, D.R. (1999). The arrangement of the three cone classes in the living human eye. Nature *397*, 520–522.

Salser, S.J., Loer, C.M., and Kenyon, C. (1993). Multiple HOM-C gene interactions specify cell fates in the nematode central nervous system. Genes Dev. *7*, 1714–1724.

Sarov, M., Murray, J.I., Schanze, K., Pozniakovski, A., Niu, W., Angermann, K., Hasse, S., Rupprecht, M., Vinis, E., Tinney, M., et al. (2014). A genome scale resource for in vivo tag-based protein function exploration in C. elegans. *150*, 855–866.

Sawa, H., and Korswagen, H.C. (2013). Wnt signaling in C. elegans. WormBook 1–30.

Schlager, B., Röseler, W., Zheng, M., Gutierrez, A., and Sommer, R.J. (2006). HAIRY-like Transcription Factors and the Evolution of the Nematode Vulva Equivalence Group. Curr. Biol. *16*, 1386–1394.

Shemer, G., and Podbilewicz, B. (2002). LIN-39 / Hox triggers cell division and represses vulval cell fusion. Genes Dev. *16*, 3136–3141.

Shemer, G., Suissa, M., Kolotuev, I., Nguyen, K.C., Hall, D.H., and Podbilewicz, B. (2004). EFF-1 is sufficient to initiate and execute tissue-specific cell fusion in C. elegans. Curr Biol *14*, 1587–1591.

Smallwood, P.M., Wang, Y., and Nathans, J. (2002). Role of a locus control region in the mutually exclusive expression of human red and green cone pigment genes. Proc. Natl. Acad. Sci. U. S. A. *99*, 1008–1011.

Smurova, K., and Podbilewicz, B. (2016). RAB-5- and DYNAMIN-1-Mediated Endocytosis of EFF-Fusogen Controls Cell-Cell Fusion. Cell Rep. *14*, 1517–1527.

Sternberg, P.W., and Horvitz, H.R. (1986). Pattern formation during vulval development in C. elegans. Cell *44*, 761–772.

Süel, G.M., Garcia-Ojalvo, J., Liberman, L.M., and Elowitz, M.B. (2006). An excitable gene regulatory circuit induces transient cellular differentiation. Nature *440*, 545–550.

Tóth, B., Ben□Moshe, S., Gavish, A., Barkai, N., and Itzkovitz, S. (2017). Early commitment and robust differentiation in colonic crypts. Mol. Syst. Biol. *13*, 902.

Ueno, S., Weidinger, G., Osugi, T., Kohn, A.D., Golob, J.L., Pabon, L., Reinecke, H., Moon, R.T., and Murry, C.E. (2007). Biphasic role for Wnt/beta-catenin signaling in cardiac specification in zebrafish and embryonic stem cells. Proc. Natl. Acad. Sci. *104*, 9685–9690.

Wang, B.B., Müller-Immergluck, M.M., Austin, J., Robinson, N.T., Chisholm, A., and Kenyon, C. (1993). A homeotic gene cluster patterns the anteroposterior body axis of C. elegans. Cell *74*, 29–42.

Wernet, M.F., Mazzoni, E.O., Çelik, A., Duncan, D.M., Duncan, I., and Desplan, C. (2006). Stochastic spineless expression creates the retinal mosaic for colour vision. Nature *440*, 174–180.

Wilkinson, H.A., Fitzgerald, K., and Greenwald, I. (1994). Reciprocal changes in expression of the receptor lin-12 and its ligand lag-2 prior to commitment in a C. elegans cell fate decision. Cell *79*, 1187–1198.

Wrischnik, L. a, and Kenyon, C.J. (1997). The role of lin-22, a hairy/enhancer of split homolog, in

patterning the peripheral nervous system of C. elegans. Development *124*, 2875–2888.

Zeev-Ben-Mordehai, T., Vasishtan, D., Siebert, C.A., and Grünewald, K. (2014). The full-length cell-cell fusogen EFF-1 is monomeric and upright on the membrane. Nat. Commun. *5*, 3912.

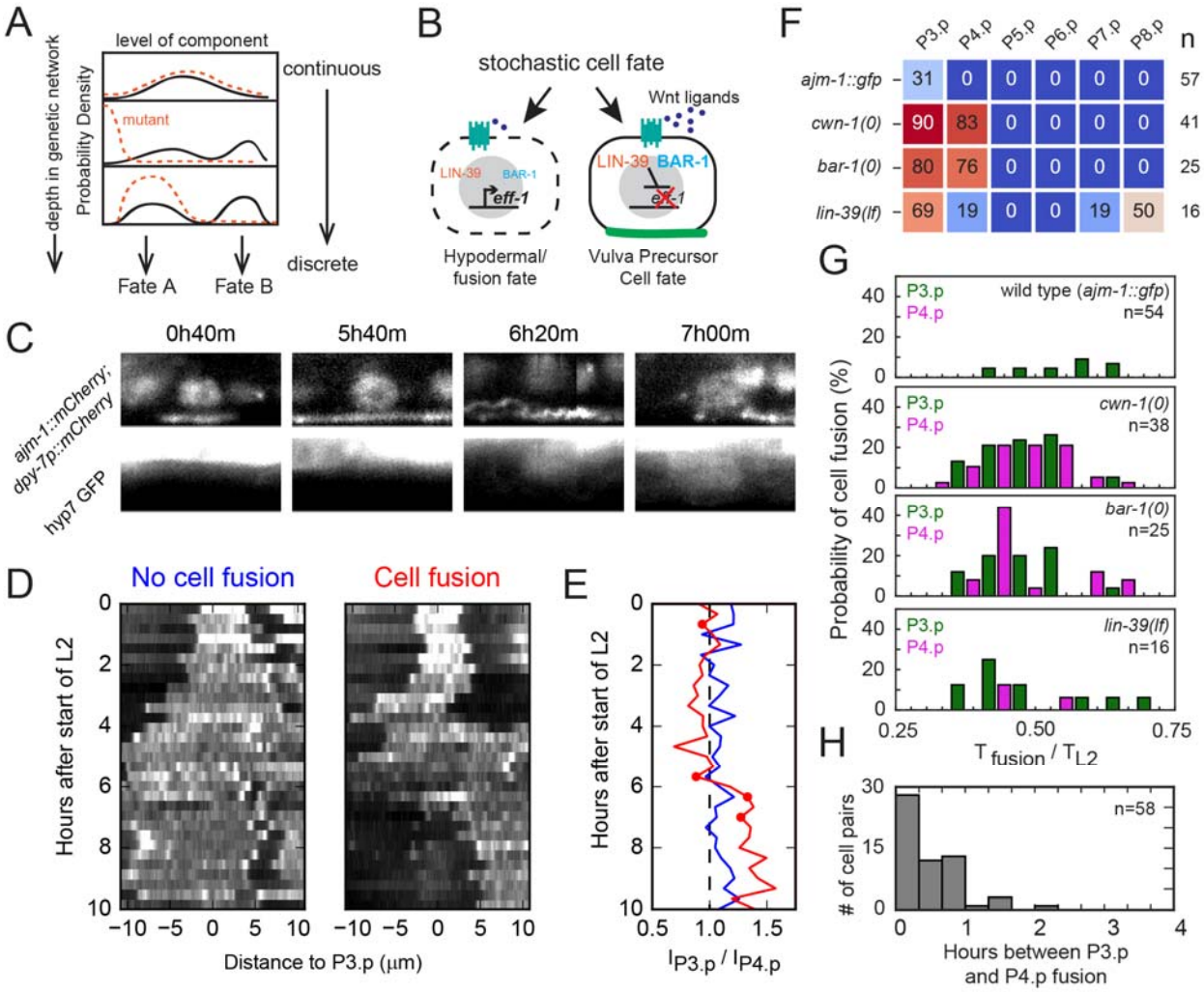

Figure 1. **Stochastic cell fate decisions in Pn.p cells.**
(A) Generic model of stochastic cell fate decisions. Continuous molecular noise is amplified by nonlinearities or feedback mechanisms in the underlying genetic network into bimodal variability (solid lines), with each peak in the bimodal distribution corresponding to a different cell fate. Relative frequency of cell fate can tuned by changing the distribution of continuous noise upstream in the signaling network (dashed lines). **(B)** Overview of the hyp7/fusion versus vulva precursor cell fate (VPC) decision. Cell assuming hyp7/fusion fate fuse (indicated by the dashed line) with the hypodermal syncytium hyp7 and lose the *ajm-1* apical junction marker (green). Cell fusion requires the expression of the fusogen *eff-1* and is inhibited by the Hox protein LIN-39 and by Wnt signaling through the β-catenin BAR-1. **(C)** Fusing P3.p cell carrying a nuclear marker (*dpy-7p:mCherry*). Upon fusion, the apical junction marker *ajm-1* retracts and GFP expressed in the hypodermal syncytium hyp7 flows into the cell. Scale bar, 5 μm. **(D)** Kymograph of *ajm-1::mCherry* fluorescence along the anteroposterior axis in a P3.p cell that assumes VPC (left panel) and hyp7/fusion fate (right panel, corresponding to the cell in (C)). In both panels, *ajm-1::mCherry* expressed in P4.p is visible on the right. **(E)** Comparing GFP inflow from the hyp7 syncytium in fusing and non-fusing cells. Shown is the ratio of GFP fluorescence intensity I between P3.p and P4.p in the same animal. The blue and red line corresponds to the

non-fusing and fusing cell in (D), respectively. Red markers correspond to the time point shown in (C). **(F)** Overview of measured hyp7/fusion frequencies in Pn.p cells in different mutant backgrounds. Mutants carried the *ajm-1::gfp* reporter except for *lin-39(0)* which carried *ajm-1::mCherry*. **(G)** Distribution of cell fusion times of P3.p (green) and P4.p cells (magenta) in different mutant backgrounds. Mutants also carried the *ajm-1::gfp* reporter, used to determine the time of fusion. Time is expressed as fraction of the L2 larval stage duration T_{L2}. The n number refers to the total number of animals examined. **(H)** Distribution of difference in cell fusion time between P3.p and P4.p cells, as measured in *cwn-1(0)*, *bar-1(0)* and *lin-39(lf)* mutant animals where both cells fuse.

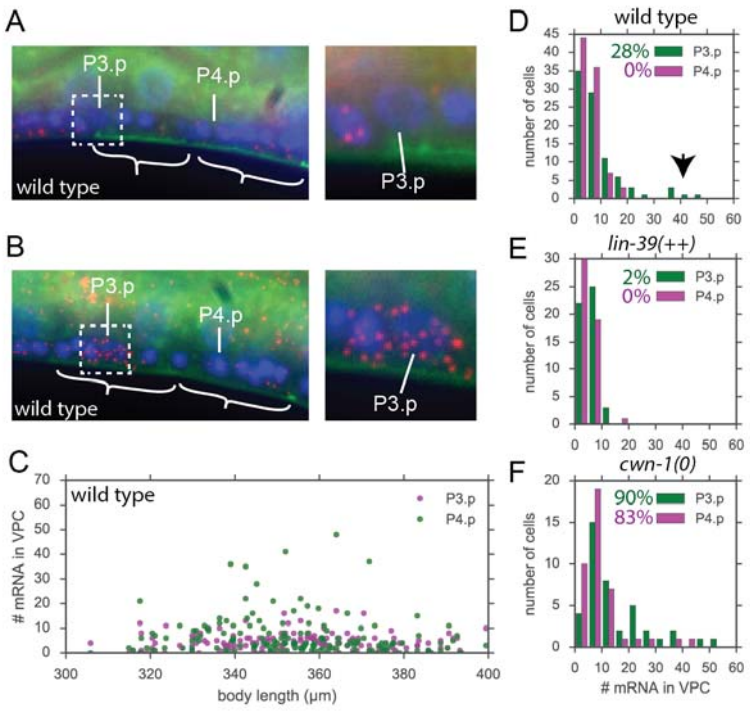

Figure 2. **Stochastic eff-1 expression in Pn.p cells**

(A) Example of *eff-1* mRNA expression preceding cell fusion in a wild-type animal. Animals were stained for single *eff-1* mRNA molecules (red), nuclei were visualized with DAPI (blue), while the cell fate is monitored with *ajm-1::gfp* (green). White brackets indicate intact apical junctions, indicating that P3.p and P4.p have not fused at this time point. The animal that has no apparent expression of *eff-1* mRNAs in the P3.p cell region. Multiple z-stacks were merged into a single image. Image on the right is zoomed in P3.p cell region. **(B)** Animal of similar age to (A), but shows high levels of *eff-1* mRNAs in the P3.p cell region **(C)** Number of *eff-1* spots as a function of worm length (as a proxy for age), considering only unfused cells. The relatively few highly expressing P3.p cells suggests that fusion proceeds rather quickly after *eff-1* expression. **(D), (E), (F)** Histograms of the distribution of the number of *eff-1* spots in unfused P3.p and P4.p cells in the wild-type and different mutants, considering only times when the cell fate decision is close to taking place (P2.p cell expressing >10 *eff-1* mRNAs). Fusion frequencies of each cell are indicated in the legend of each histogram. The black arrow in the wild-type histogram shows the small population of cells expressing high levels of *eff-1* (bimodality).

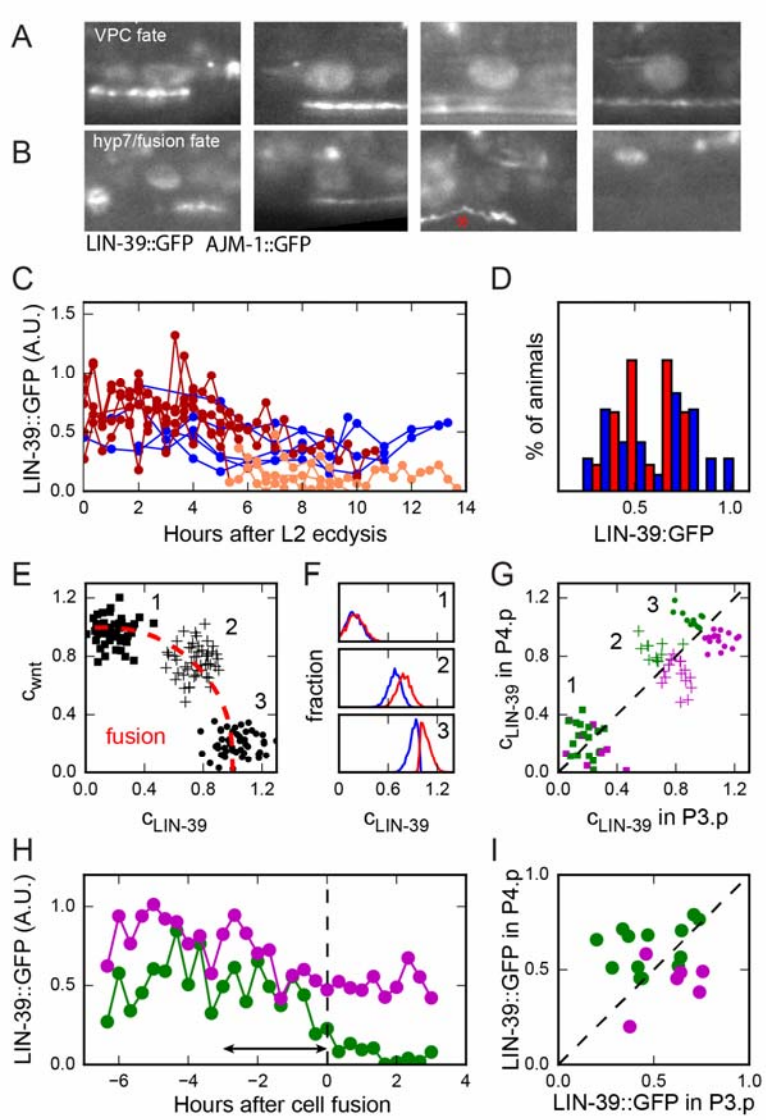

Figure 3**. Variability in LIN-39 protein level.**

(A), (B) Image sequence of a cell assuming (A) VPC or (B) hyp7/fusion fate. Nuclear LIN-39 levels are visualized using a LIN-39::GFP protein fusion, while cell fusion is determined using an *ajm-1::GFP* reporter. The red star indicates the first time point at which AJM-1 retraction occurs, indicating cell fusion has occurred. **(C)**. Nuclear LIN-39 fluorescence in fusing (red) and non-fusing (blue) P3.p cells. For fusing P3.p cells, color distinguishes time point prior to (dark red) and after fusion (light red). **(D)** Distribution of nuclear LIN-39 fluorescence in fusing (red) and non-fusing (blue) P3.p cells. In fusing cells, fluorescence was averaged over 3 hour window directly prior to fusion, whereas in non-fusing cells a time window of 3 hours prior to the average time of cell fusion was used. **(E)**. Model of inhibition of *eff-1* expression and hyp7/fusion fate by Wnt signaling and LIN-39 (Eq. 1 in Methods). Fusion occurs in the region (indicated by the dashed red line) with sufficiently low Wnt signaling (c_{wnt}) and LIN-39 levels ($c_{\mathrm{LIN\text{-}39}}$). Markers are individual simulations of three scenarios, where (1) the cell fate decision is dominated by variability in Wnt levels (squares), (2) equally impacted by variability in Wnt and LIN-39 levels (crosses), or (3) dominated by variability in LIN-39 levels (circles). **(F)** Distribution of LIN-39

levels in the model for cells that fuse (red) or assume VPC fate (blue), for each of the scenarios in (E). **(G)** LIN-39 levels in P3.p and P4.p for simulations in which P3.p assumes hyp7/fusion fate and the P4.p assumes VPC fate (green) or the reverse (magenta), for each of the scenarios in (E). **(H)** Nuclear LIN-39 fluorescence in P3.p (green) and P4.p (magenta) in an animal in which P3.p, but not P4.p, assumes hyp7/fusion fate. The arrow indicates the time window over which LIN-39 fluorescence is averaged in (D) and (I). The dashed line indicates the time of fusion. **(I)** Nuclear LIN-39 fluorescence levels in P3.p and P4.p for animals in which P3.p assumes hyp7/fusion fate and the P4.p assumes VPC fate (green) or the reverse (magenta). Each marker corresponds to a single animal and is averaged over a 3 h time window prior to cell fusion.

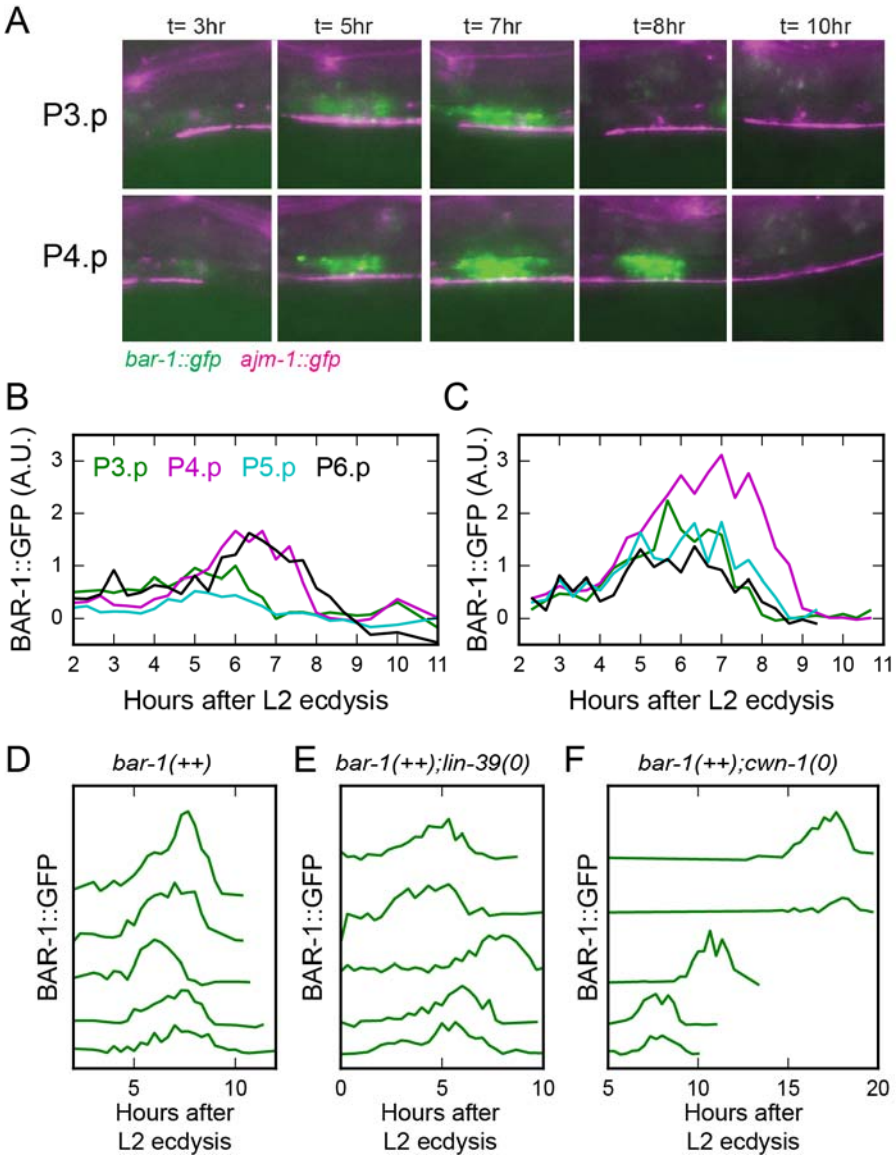

Figure 4. **Pulsatile BAR-1 dynamics during cell fate decision.**

(A) Image sequence of the BAR-1::GFP dynamics (green) over time in P3.p and P4.p cells in the same animal, with both cells assuming VPC fate. Animals also carry the *ajm-1::mCherry* marker (magenta). **(B),(C)** Dynamics of cellular BAR-1::GFP fluorescence in P(3-6).p cells in two different animals. **(D)-(F)** BAR-1::GFP dynamics in P3.p cells in (D) *bar-1(++)*, (E) *bar-1(++);lin-39(lf)*, (F) *bar-1(+); cwn-1(0)* animals. Traces for different animals are shifted along the vertical axis for clarity.

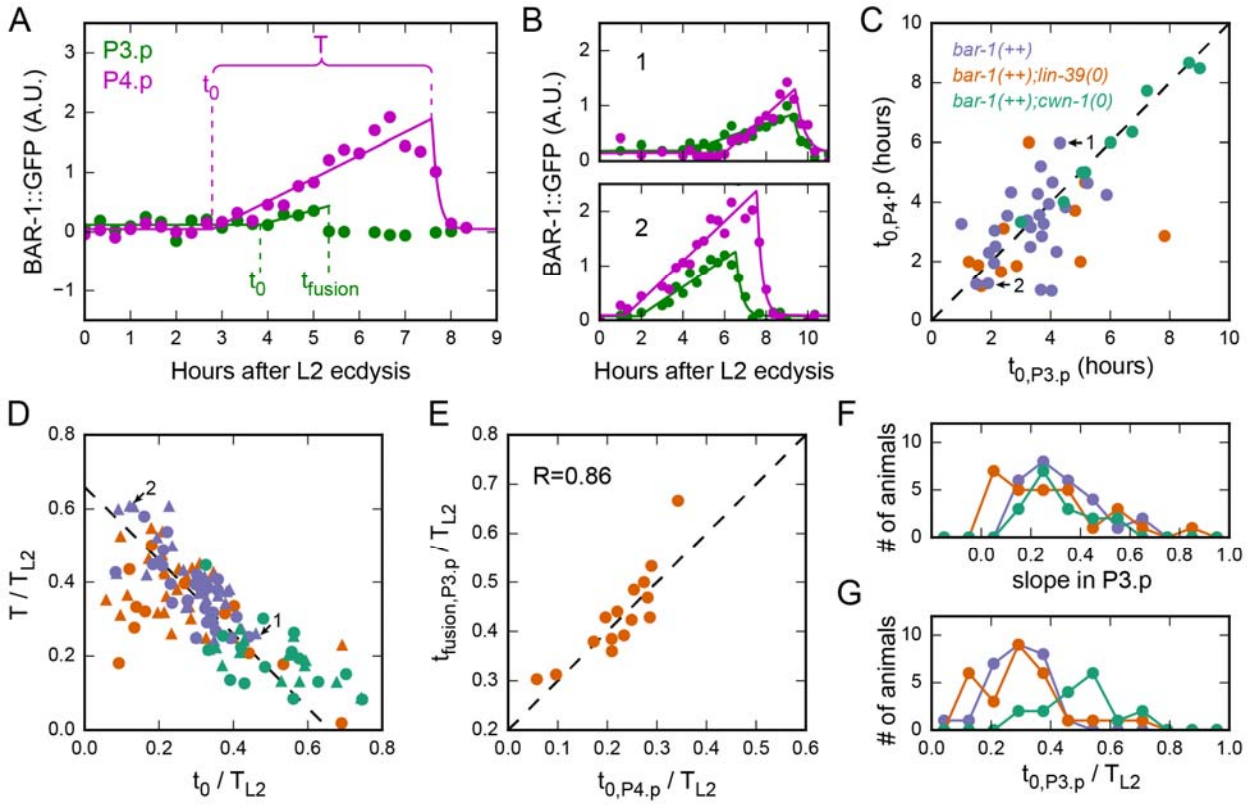

Figure 5. **Variability in BAR-1 pulse dynamics.**

(A) Quantifying BAR-1 pulse dynamics. Marker correspond to measured BAR-1::GFP levels in P3.p (green) and P4.p (magenta) for an animal in which P3.p, but not P4.p, assumes hyp7/fusion fate. Solid lines represent a model of BAR-1 accumulation dynamics (Eq. 3 in the Methods). Using the model, each BAR-1 accumulation pulse can be described by three key parameters: pulse onset time t_0, pulse slope s and pulse duration T (for non-fusing VPCs) or time of fusion t_{fusion} (for hyp7/fusion cells). **(B)** Examples of animals showing differences in (relative) timing of BAR-1 accumulation pulses. **(C)** Correlation in pulse onset time t_0 between P3.p and P4.p cells in the same animal. Each marker corresponds to a single animal, with color indicating *bar-1(++)* (purple), *bar-1(++);lin-39(lf)* (orange) and *bar-1(++);cwn-1(0)* mutants (green). Animals were selected where neither P3.p nor P4.p fused. Arrows indicate the animals in (B). **(D)** Correlation between pulse onset time t_0 and pulse duration T in non-fusing P3.p (circles) and P4.p cells (triangles). Color indicates the different mutant backgrounds in (C) and arrows indicate the animals in (C). Time is expressed as fraction of the L2 larval stage duration T_{L2}. The dashed line is $T/T_{\mathrm{L2}} = 0.66 - t_0/T_{\mathrm{L2}}$. **(E)** Correlation between pulse onset time t_0 in P4.p and fusion time t_{fusion} in P3.p, in *bar-1(++);lin-39(lf)* animals where P3.p, but not P4.p, assume hyp7/fusion fate. The dashed line is $t_{\mathrm{fusion}}/T_{\mathrm{L2}} = 0.2 + t_0/T_{\mathrm{L2}}$. **(F), (G)** Distribution of (F) pulse onset time t_0 and (G) pulse slope s in P3.p cells. Color indicates the different mutant backgrounds in (C). Data for P3.p cells that assume hyp7/fusion and VPC fate is pooled.

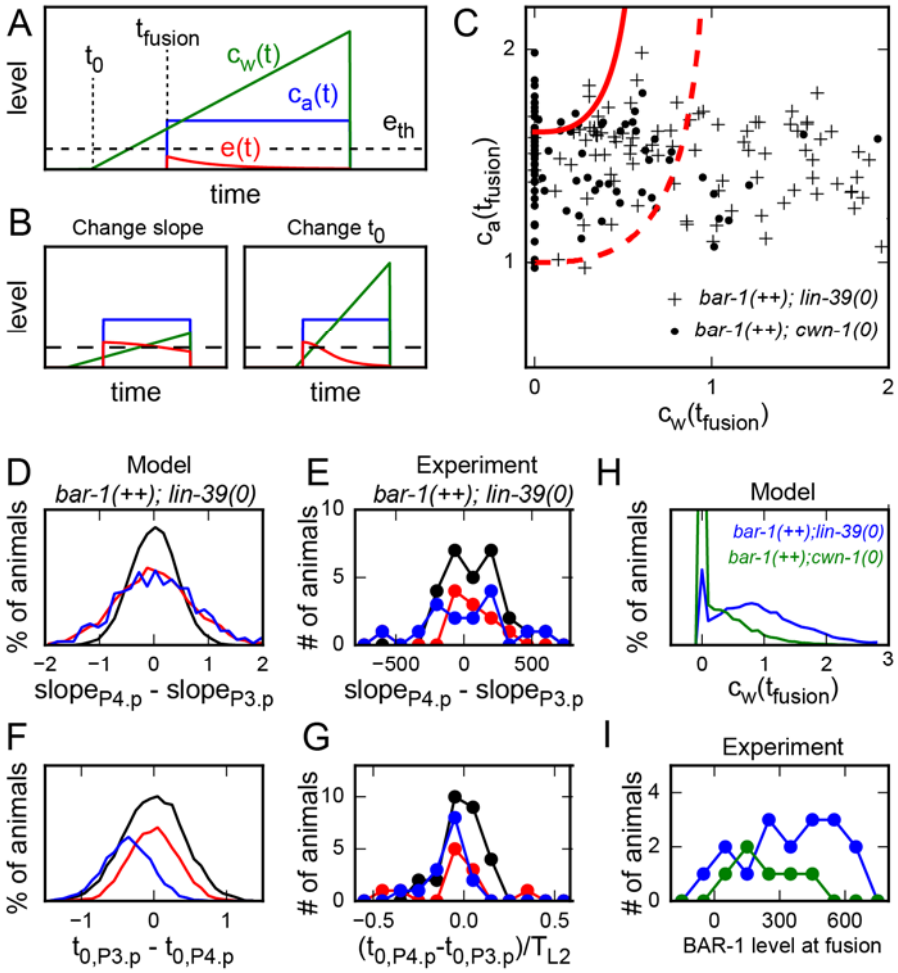

Figure 6. **Cell fate bias by BAR-1 pulse dynamics.**
(A) Model of inhibition of *eff-1* expression level $e(t)$ (red line) and hyp7/fusion fate by a pulsatile Wnt signaling level $c_{\mathrm{wnt}}(t)$ (green line) (Eq. 2 in Methods). Cell fusion is activated at time t_{fusion}, but only occurs if the activation level c_a (blue line) is high enough and the Wnt inhibition $c_{\mathrm{wnt}}(t)$ is low enough that *eff-1* is expressed above a threshold level e_{th} (dashed line). **(B)** In this model, fusion frequency can be changed both by changing the slope (left panel) and onset time (right panel) of BAR-1 pulses. **(C)** Model simulations of cell fate decisions in different mutant backgrounds. For wild-type animals, hyp7/fusion fate occurs in a small region (demarcated by the solid red line). Upon removal of the inhibitor LIN-39 this region is expanded (dashed red line). Crosses correspond to individual simulations for animals with elevated BAR-1 levels (*bar-1(++)* and *bar-1(++);lin-39(lf)*) and circles to simulations with BAR-1 levels closer to wild type (*bar-1(++); cwn-1(0)*). **(D),(E)** Distribution of the difference in pulse slope s for BAR-1 pulses in P3.p and P4.p, both for the (D) model and (E) experiments. Shown are distributions for *bar-1(++)* animals (black line), where no Pn.p cells fuse, and *bar-1(++);lin-39(lf)* animals where P3.p, but not P4.p, fused (blue line) or where neither P3.p nor P4.p fused (red line). In all cases, pulse slope does not bias the cell fate decision. **(F),(G)** Distribution of the difference in pulse onset time t_0 for BAR-1 pulses in P3.p and P4.p, both for the (F) model and (G) experiments. Line color indicates mutant background as in (D) and (E). For the experimental data, time is

expressed as fraction of the L2 larval stage duration T_{L2}. Late pulse onset biases towards hyp7/fusion fate. **(H), (I)** Comparing BAR-1 levels at the time of cell fusion between *bar-1(++);lin-39(lf)* (blue) and *bar-1(++);cwn-1(0)* animals (green), both for the (H) model and (I) experiments. For the experiments, data for P3.p and P4.p cells was pooled. BAR-1 levels at time of fusion are higher in *bar-1(++);lin-39(lf)* animals.

Supplementary Table 1. **Pn.p fusion frequencies in different genetic backgrounds**

	Fusion rates (%) [a]						
Genotype	P3.p	P4.p	P5.p	P6.p	P7.p	P8.p	**N**
ncIs13[ajm-1::GFP] [b]	28	0	0	0	0	0	**57**
ouIs20[ajm-1::mCherry] [b]	37	0	0	0	0	0	**30**
cwn-1(ok546);ncIs13[ajm-1::GFP] ***cwn-1(0)***	90	83	0	0	0	0	**41**
bar-1(ga80);ncIs13[ajm-1::GFP] ***bar-1(0)***	80	76	4	0	0	4	**25**
lin-39(gk893);ncIs13[ajm-1::GFP] [c] ***lin-39(0)***	100	100	100	100	100	100	**17**
lin-39(n709);ouIs20[ajm-1::mCherry] ***lin-39(lf)***	69	19	0	0	19	50	**16**
lin-39::GFP;HIS24-H2B::mCherry; ncIs13[ajm-1::GFP] ***lin-39(++)***	2	0	0	0	0	0	**48**
cwn-1(ok546);lin-39::GFP;HIS24-H2B::mCherry;ncIs13[ajm-1::GFP] ***cwn-1(0); lin-39(++)***	20	14	1	0	0	0	**126**
bar-1::GFP;ouIs20[ajm-1::mCherry] ***bar-1(++)***	0	0	0	0	0	0	**30**
bar-1::GFP;cwn-1(ok546);ouIs20[ajm-1::mCherry] ***cwn-1(0); bar-1(++)***	6	8	0	0	0	0	**64**
bar-1::GFP;lin-39(n709);ouIs20 [ajm-1::mCherry] ***lin-39(lf); bar-1(++)***	24	4	3	0	13	19	**70**

[a] Fusion rates are rounded to the nearest percentage. Fusion events were counted by the loss of *ajm-1* staining during the L2 stage, and non-fusion animals were only counted if the animal reached the L3 ecdysis without a fusion event.

[b] No statistical difference between P3.p fusion rates in these marker strains, (P= 0.47, Fisher's Exact Test).

[c] P3.p – P8.p fused prematurely during the L1 stage in the null mutant.